

# Unveiling Inequality of Atoms in Ultrasmall Pt Clusters: Oxygen Adsorption Limited to the Uppermost Atomic Layer

Federico Loi, Luca Bignardi, Deborah Perco, Andrea Berti, Paolo Lacovig, Silvano Lizzit, Aras Kartouzian, Ulrich Heiz, Dario Alfè, and Alessandro Baraldi\*

The concept of preferential atomic and molecular adsorption site is of primary relevance in heterogeneous catalysis. In the case of ultrasmall size-selected clusters, distinguishing the role played by each atom in a reaction is extremely challenging due to their reduced size and peculiar structures. Herein, it is revealed how the inequivalent atoms composing graphene-supported Pt<sub>12</sub> and Pt<sub>13</sub> clusters behave differently in the photoinduced dissociation of O<sub>2</sub>, with only those in the uppermost layer of the clusters being involved in the reaction. In this process, the epitaxial graphene support plays a fundamental active role: its corrugation and pinning induced by the presence of the clusters are crucial for defining the preferential adsorption site on the Pt atomic agglomerates, facilitating the lateral diffusion of physisorbed oxygen at a distance that induces its selective adsorption in the topmost layer of the clusters, and inducing an inhomogeneous charge distribution within the clusters which directly affects the O<sub>2</sub> adsorption. The inhomogeneous oxidation of the clusters is resolved by means of synchrotron-based X-ray photoelectron spectroscopy and supported by ab initio density functional theory calculations. The possibility to identify the active sites on Pt clusters induced by cluster–support interactions has the potential to enhance the experimentally supported design of nanocatalysts.

physical properties of atoms confined in their outermost layers. The concept of undercoordination associated with surface atoms<sup>[1]</sup> becomes particularly relevant when considering atomic aggregates such as nanoparticles, for which it has been highlighted that the presence of nonequivalent atoms on their facets generates different adsorption configurations associated with a highly varied chemical reactivity.<sup>[2]</sup> However, when the particle size reaches the subnanometric scale, the concept of surface becomes more elusive because the ratio between the number of surface and bulk atoms formally tends to infinity. Furthermore, on the subnanometric scale, the crystalline structure typical of larger nanoparticles, a few nanometers in size, fades away<sup>[3]</sup> and they become difficult to distinguish using common characterization techniques.<sup>[4]</sup> Even with the application of synchrotron-based experimental techniques, which greatly outperform conventional ones in terms of sensitivity and resolution, it is possible to obtain only aver-

aged information on the nonequivalent atoms composing the clusters.<sup>[5–7]</sup> This fact poses a significant challenge for atomic-level investigations of adsorption, dissociation, and chemical reaction processes taking place at the surface of ultrasmall clusters,<sup>[8,9]</sup> limiting the rational design of cluster-based catalysts.

## 1. Introduction

The role played by solid surfaces in a broad set of physical phenomena has been the subject of numerous investigations in the last decades, aimed at highlighting the unique chemical and


F. Loi,<sup>[†]</sup> L. Bignardi, D. Perco, A. Berti, A. Baraldi  
Department of Physics  
University of Trieste  
via Valerio 2, 34127 Trieste, Italy  
E-mail: alessandro.baraldi@elettra.eu

P. Lacovig, S. Lizzit, A. Baraldi  
Elettra Sincrotrone Trieste  
AREA Science Park  
Basovizza, 34149 Trieste, Italy

A. Kartouzian, U. Heiz  
Chemistry Department & Catalysis Research Center  
Technical University of Munich  
Lichtenbergstr. 4, D-85748 Garching, Germany

D. Alfè  
Department of Earth Sciences and London Centre for Nanotechnology  
University College London  
Gower Street, London WC1E 6BT, UK

D. Alfè  
Dipartimento di Fisica Ettore Pancini  
Università di Napoli Federico II, Monte S. Angelo  
80126 Napoli, Italy

 The ORCID identification number(s) for the author(s) of this article can be found under <https://doi.org/10.1002/sstr.202400250>.

<sup>[†]</sup>Present address: Department of Nanocatalysis, J. Heyrovsky Institute of Physical Chemistry, Dolejskova 2155/73, Prague 182 23, Czech Republic

© 2024 The Author(s). Small Structures published by Wiley-VCH GmbH. This is an open access article under the terms of the Creative Commons Attribution License, which permits use, distribution and reproduction in any medium, provided the original work is properly cited.

DOI: 10.1002/sstr.202400250

The case of Pt is particularly significant, as this metal is widely employed, from nanocatalysis<sup>[10–14]</sup> to electrochemistry<sup>[15–17]</sup> and more recently also in the shape of atomically dispersed single atoms<sup>[4,18–23]</sup> and supported metallic clusters.<sup>[6,24–30]</sup> Large efforts have been made to modify the morphology of Pt nanocrystals' surfaces with the aim of increasing chemical reactivity and selectivity.<sup>[31–33]</sup> Among the various surface mechanisms that are crucial for Pt-based catalysts, oxidation stands out as particularly significant. This is motivated by the numerous chemical reactions involving platinum occurring in an oxygen-rich atmosphere<sup>[34–36]</sup> and by means of oxide supports that can boost the oxygen transfer on the Pt nanoparticles.<sup>[37]</sup> For instance, theoretical calculations have revealed that the chemical reactivity of oxidized Pt nanoclusters can exceed that of individual Pt atoms by 100–1000 times.<sup>[38]</sup> Additionally, their unique properties can be significantly influenced by their interaction with the support material.<sup>[39]</sup> The possibility to employ oxidized Pt clusters to effectively suppress the hydrogen oxidation in photocatalytic water splitting just by pushing the catalyst in a higher oxidation state constitutes another appealing aspect.<sup>[40]</sup> However, understanding the oxygen adsorption site on a Pt cluster is complicated by the fact that clusters formed by a small number of atoms can coexist with numerous nonequivalent adsorption configurations,<sup>[41]</sup> often impossible to resolve experimentally even with state-of-the-art synchrotron-based techniques.<sup>[42]</sup> In addition, the influence and interaction with the support can play an even more significant role compared to the case of nanoparticles. Determining the spatial distribution of reactants and more specifically the location where oxygen atoms bind to a subnano atomic aggregate is thus extremely challenging.

In this work, we show that oxygen atoms markedly do not occupy the surface of Pt clusters supported on graphene with a stochastic arrangement but are preferentially adsorbed onto the topmost atomic Pt layer. This effect is the result of a synergistic interplay between the supported clusters and the epitaxial

graphene, with the latter playing an active role in modifying the electronic properties of the Pt atoms composing the clusters and finally determining their activity depending on the distance from the substrate. Our investigation relies on the possibility to produce and deposit mass-selected atomic clusters on a graphene substrate and to study their properties in situ using a combined theoretical and experimental approach to resolve nonequivalent atoms in the cluster. Our outcomes are valid for both Pt clusters composed of 12 and 13 atoms, the former being known for their high electrochemical reactivity while the latter being a stable cluster with a magic number of atoms.<sup>[43]</sup> Pt clusters with this nuclearity are considered to be important materials to improve the electrochemical activity for the four-electron reduction of oxygen molecules,<sup>[44]</sup> which is a fundamental chemical process for various industrial applications such as the cathode reaction of a fuel cell. The interest in studying also nonmagic number subnanometer clusters is that they may have local atomic configurations that are unavailable on bulk or larger nanoparticles.<sup>[45]</sup>

## 2. Results and Discussion

As a first step, the size-selected clusters were produced and deposited in situ on the graphene/Ir(111) interface kept at 40 K on a spot of about 5 mm diameter with a total atomic coverage of 1% ML calculated with respect to the Ir(111) surface, for a total of  $\approx 3 \times 10^{13}$  clusters. With this coverage, the average cluster-cluster distance on the surface is  $\approx 5$  nm. Subsequently, we have carried out high-resolution X-ray photoelectron spectroscopy (HRXPS) experiments on the freshly deposited clusters. The Pt 4f core-level spectra acquired after the deposition of Pt<sub>12</sub> and Pt<sub>13</sub> clusters at 40 K are shown in **Figure 1a,b**. The line shape appears very similar in both cases and exhibits the  $j = 5/2$  and  $7/2$  spin-orbit doublet separated by  $3.34 \pm 0.02$  eV, with the same binding energy (BE) of the  $4f_{7/2}$  component within the

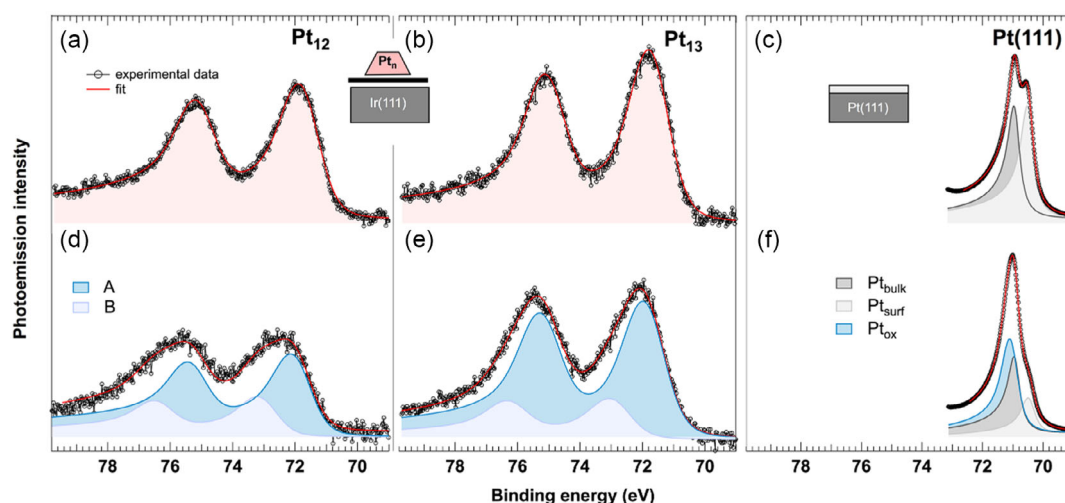


**Figure 1.** a,b) High-resolution Pt 4f core-level spectra corresponding to a,b) as-deposited size-selected Pt<sub>12</sub> and Pt<sub>13</sub> clusters on Gr/Ir(111); c)  $4f_{7/2}$  spectrum of the Pt(111) clean surface for comparison; d,e) Pt<sub>12</sub> and Pt<sub>13</sub> cluster after 1L O<sub>2</sub> exposure at 20 K and photon-induced dissociation fitted with two components A and B originating from different degrees of oxidation (see main text); and f)  $4f_{7/2}$  spectrum of Pt(111) surface after oxygen exposure and formation of a  $p(2 \times 2)$  oxygen structure at 0.25 ML. All the spectra were acquired with a photon energy of 250 eV.

experimental error bar ( $BE = 71.69 \pm 0.05$  for  $Pt_{12}$  and  $71.65 \pm 0.05$  for  $Pt_{13}$ ). The spectra were fit with Doniach–Šunjić line profiles (see Experimental Section for details). Very similar parameters for the Gaussian ( $1.13 \pm 0.05$  eV for  $Pt_{12}$  and  $1.12 \pm 0.05$  eV for  $Pt_{13}$ ) and the Lorentzian ( $0.35 \pm 0.02$  eV for  $Pt_{12}$  and  $0.35 \pm 0.02$  eV for  $Pt_{13}$ ) contributions are extracted from the spectral analysis. The only difference concerns the asymmetry parameter, which is  $0.28 \pm 0.03$  for  $Pt_{12}$ , significantly larger than for  $Pt_{13}$  ( $0.21 \pm 0.02$ ). The reason for this difference can be found in the different electron densities of states at the Fermi energy, which results in a different probability of exciting electron–hole pairs. The different line shapes as a function of cluster size in the two  $Pt4f$  spectra support the fact that the mass selection is preserved upon deposition. In addition, it is possible to appreciate specific diversity of clusters with respect to bulk matter or solid surfaces by comparing our results with the spectrum obtained for the  $4f_{7/2}$  core level in the case of  $Pt(111)$ , displayed in Figure 1c, which shows two components originating from the emission from bulk and surface atoms.<sup>[46]</sup> The  $Pt_{bulk}$  bulk component (dark gray), caused by atoms with atomic coordination  $n = 12$ , is positioned at  $70.92 \pm 0.05$  eV, almost 1 eV lower in BE than the clusters. Such a case provides a compelling example of the different behaviors between clusters and bulk material, attributed to different effects such as variations in interatomic distances, charge transfer processes with the substrate, and contribution of core-hole screening.<sup>[47–49]</sup> Another significant difference between clusters and  $Pt(111)$  can be found in the Gaussian broadening which is greater than 1.1 eV for Pt clusters, despite the energy resolution used for measuring all the spectra being the same and equal to 50 meV. This result is primarily due to the large number of local configurations of Pt atoms forming a cluster, but also to possible differences in cluster landing orientation on the substrate and the presence of isomers.<sup>[50]</sup>

The adsorption of oxygen atoms on the clusters was achieved using the same photodissociation strategy employed in the case of  $Ag^{[42]}$  and  $Fe^{[48]}$  clusters. The exposure of  $O_2$  at 40 K leads to a physisorption state which, upon soft X-ray irradiation and consequential production of secondary electrons, results in the breakup of the O–O bond and formation of atomic oxygen. The effectiveness of this method in the case of Pt was also validated through an experiment conducted on  $Pt(111)$ , where it was demonstrated that even the superoxide ( $O_2^-$ ) weakly chemisorbed intermediate species, formed after exposure to molecular oxygen at 80 K,<sup>[51]</sup> convert to atomic oxygen due to prolonged exposure to a soft X-ray photon flux (see Figure S1, Supporting Information).

The  $4f$  core-level spectra of  $Pt_{12}$  and  $Pt_{13}$  clusters obtained after exposing them to 1L ( $p = 2 \times 10^{-9}$  mbar of molecular oxygen for 11 min and 5 s) are shown in Figure 1d,e and exhibit a significant modification in the spectral line shape, with broadening toward higher BEs, a fingerprint of atomic oxygen adsorption.<sup>[51]</sup>

In both spectra, two components emerge from the spectral analysis, suggesting the presence of two different families of atoms (labeled A and B) with different oxidation states in the clusters. In the case of  $Pt_{12}$  (reported in Figure 1d), the first peak corresponding to the  $4f_{7/2}$  component (A), which accounts for 70% of the spectral intensity, is centered at  $72.03 \pm 0.05$  eV, while the second component (B) is found at

$BE = 73.21 \pm 0.05$  eV. If compared to metallic spectra, these components show a core-level shift of  $0.3 \pm 0.1$  and  $1.5 \pm 0.1$  eV, respectively. The same trend is also obtained from the analysis of the  $Pt_{13}$  spectrum, with the two components centered at  $71.86 \pm 0.05$  and  $72.94 \pm 0.05$ , with a ratio of 4:1 in favor of the lower-energy component (shifts of  $0.2 \pm 0.1$  and  $1.3 \pm 0.1$  eV).

As a first step to understanding the local configuration and oxidation state that generate the A and B components, we can compare these results with the shifts induced by oxygen adsorption on different Pt-based interfaces. In the case of  $Pt(111)$ , a low coverage of chemisorbed O forms a  $p(2 \times 2)$  long-range ordered structure and induces a core-level shift of +590 meV with respect to the clean surface component (see Figure 1f). In the case of Pt surfaces, new additional components are obtained only for exposures to high oxygen pressures, leading to the formation of  $PtO$ , typically associated with BEs of 72–72.7 eV,<sup>[35]</sup> and subsequently  $PtO_2$ , identified by the growth of a component at 73.7–74.1 eV.<sup>[35,52]</sup> The BEs of the B components in Figure 1d, e, (73.0–73.2 eV) are, for both  $Pt_{12}$  and  $Pt_{13}$ , in between the values associated with  $PtO$  and  $PtO_2$ , suggesting an intermediate degree of oxidation such as in the bulk phase  $Pt_3O_4$ , where Pt has the nominal oxidation state  $8/3+$ .<sup>[53]</sup> A BE close to 73 eV was observed also at the atomic steps of oxidized  $Pt(332)^{[54]}$  and  $Pt(557)$  surfaces<sup>[55]</sup> with the formation of local  $PtO_4$  geometry similar to the one composing the  $PtO$  and  $Pt_3O_4$  bulk oxides. This structure was defined as 1D  $PtO_2$  stripe, and it was proposed to be a precursor phase to the complete oxidation of Pt surfaces. Since this structure emerges on undercoordinated atoms such as steps and kinks,<sup>[52]</sup> it was proposed that a similar one may appear also in the case of Pt nanoparticles due to the high density of undercoordinated sites. On the contrary, the BE of A and its core-level shift of  $<0.3$  eV with respect to the metallic clusters suggest the presence of atoms with an oxidation state lower than one. However, it is not straightforward to directly compare the values of BE for surface and clusters, because of the effects mentioned earlier which influence markedly the metallic clusters but cannot be completely ruled out in the case of oxidized ones. Given the exceedingly low cluster coverage in our experiment (approximately one cluster per 3000 carbon atoms), a measure essential for preventing cluster agglomeration and preserving the mass selection, it becomes challenging to discern the changes caused by the clusters on the graphene C 1s spectrum, as observed in the case of larger adsorbate coverages such as 0.05 ML of  $CO^{[56]}$  or on the O 1s signal originating from adsorbed oxygen from the oxidized clusters. For a rigorous interpretation of the experimental results, we then relied on density functional theory (DFT) calculations first to study the adsorption configurations of the clusters on the graphene support and then to analyze their oxidation in comparison with the experimental spectra.

Figure 2 depicts simulated structures for  $Pt_{12}$  and  $Pt_{13}$  clusters (left and right columns respectively) with four different adsorption orientations ( $R_1$ – $R_4$ ) on the graphene/Ir(111) interface. The minimum energy configuration of the charged cluster, obtained by considering the free-standing cluster in the gas phase, was used as standard configuration to minimize the energy of the neutralized cluster interacting with graphene in the hexagonal-close-packed (HCP) regions of the Moiré cell

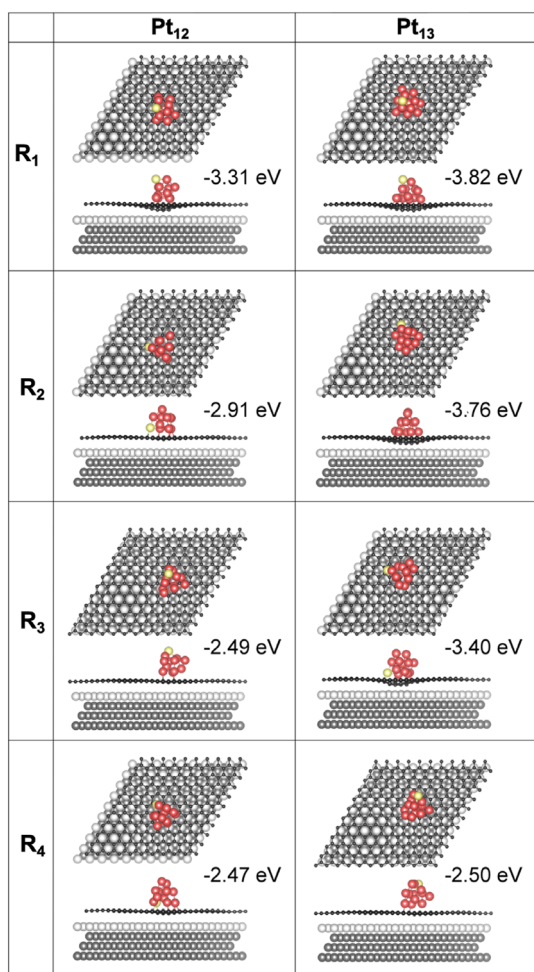


**Figure 2.** Top and side views of the Gr/Ir unit cell with the different adsorption configurations (from  $R_1$  to  $R_4$ ) of  $Pt_{12}$  and  $Pt_{13}$  clusters. Light and medium gray are used for surface and Ir bulk atoms, respectively; black stands for C; and red is used for Pt. In the structural models, a single Pt atom is highlighted in yellow to provide a reference for the cluster rotation. Adsorption energies are referred with respect to the cluster energy at infinity.

formed by graphene on Ir(111), which is known to correspond to the minimum energy configuration for atoms and clusters.<sup>[57]</sup> A specific Pt atom is highlighted in yellow in all the panels to provide a visual reference to compare the changes in orientation of the clusters. The adsorption geometry significantly influences the cluster stability, as evident from the adsorption energies which vary by several hundredths eV. For both  $Pt_{12}$  and  $Pt_{13}$ , the preferred configurations induce a strong deformation of the graphene lattice, which undergoes pinning toward the metallic substrate. A similar effect has already been highlighted in the case of graphene-supported small Ir and Pt flat adislands that can strongly interact with the metallic substrate and not only modify the geometry of graphene but also induce a rehybridization of the carbon atoms from  $sp^2$  to  $sp^3$  diamond-like bonding.<sup>[58–60]</sup> A comparable trend takes place also in the case of Pt clusters supported on defective free-standing graphene<sup>[61]</sup> and in defective graphene on a Pt surface, with the involved charge transfer

that can affect the stability and activity of the Pt/graphene catalyst in the oxygen reduction reaction.<sup>[62]</sup> The favored adsorption configurations ( $-3.31$  eV for  $Pt_{12}$  and  $-3.82$  eV for  $Pt_{13}$ ) correspond to the  $R_1$  rotations shown in Figure 2, where the distance of the cluster (centroid coordinate of the cluster) from the first atomic layer of the Ir(111) surface is minimal and corresponds to 6.5 and 6.1 Å for  $Pt_{12}$  and  $Pt_{13}$ , respectively (see Figure S2, Supporting Information).

In order to draw a comparison with the experimental findings, we determined the BE of the Pt 4f core electrons (see bar codes in Figure 3), including final state effects, of each atom of the clusters for each orientation on the support, for a total of 100 CLSs.

The absolute values of the core-level BEs obtained from the calculations cannot be compared directly to measurable quantities, but the CLSs can usually be obtained with an accuracy of a few tens of meV.<sup>[63]</sup> Absolute core-level BEs are shifted using an offset parameter which is obtained by fitting the experimental spectrum with the four different components originating from

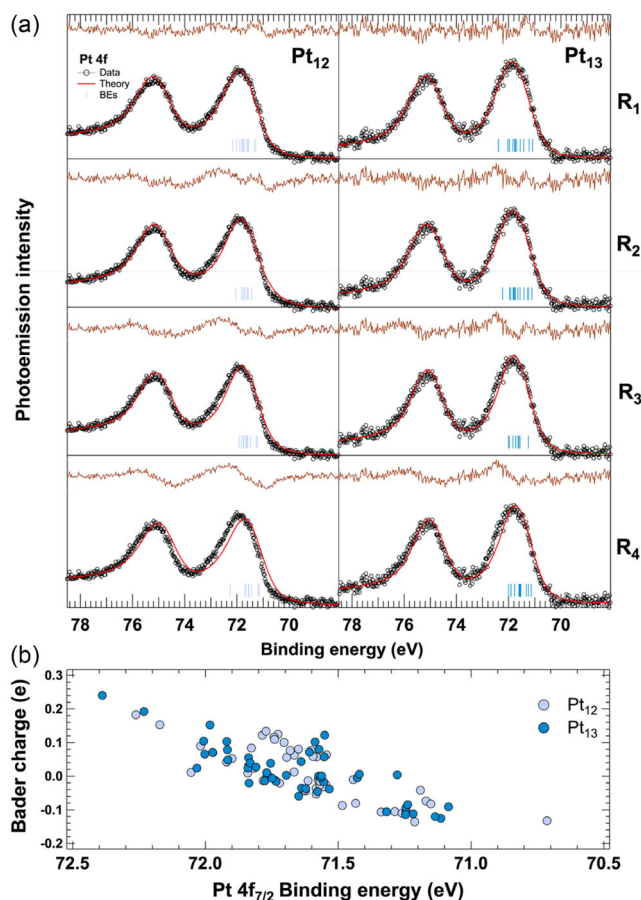


**Figure 3.** a) High-resolution Pt 4f core spectra of the clean  $Pt_{12}$  (left column) and  $Pt_{13}$  clusters on Gr/Ir(111) and the corresponding fitting curves obtained using the DFT calculated  $4f_{7/2}$  core-electron BEs of each atom of the cluster in the different orientational configurations ( $R_1$ – $R_4$ ). The red lines through the spectra are the results of the linear least-square fits to the data points. The residuals of the fit are also shown in the top part of each panel (brown curves). b) Relationship between calculated Bader charge and calculated core-electron BE for the atoms belonging to the  $Pt_{12}$  and  $Pt_{13}$  clusters for all orientations displayed in Figure 2.



the configurations  $R_1$ – $R_4$  (Figure S3, Supporting Information). The result of this analysis can be also used to determine the relative abundance of each component. In the case of  $Pt_{13}$ , 90% of the spectral weight can be attributed to clusters with  $R_1$  orientation, consistent with the minimum energy values obtained from DFT calculations. At this point, with the obtained absolute Bes, each model can be compared directly to the experimental spectra (Figure 3a), where the fitting residuals and chi-squared analysis are consistent with the calculated adsorption energies (see Figure S4, Supporting Information). The value of the offset parameter thus obtained with this fit was used in the subsequent analysis to align the theoretical core-level energies to all the experimental spectra.

The distribution of  $4f_{7/2}$  core-electron BEs is  $\approx 1$  eV wide for both clusters, ranging from about 71.1 to 72.1 eV, with a few scattered points. The BEs of all the atoms in the different configurations are reported in Figure S5, Supporting Information. A similar distribution of the  $4f_{7/2}$  BEs has been reported for small 2D Pt islands on the Gr/Ir interface. The distribution originates from Pt atoms in different positions in the island, that is, at the center, at the edges, or in between.<sup>[64]</sup> It is interesting to note that for the least preferred configurations, there is only a weak statistical correlation between the BE of the core electrons calculated for each of the atoms composing the clusters and their distance from the Ir(111) surface layer (see Figure S6, Supporting Information), which is, on the other hand, well correlated with the clusters adsorption energy, as discussed earlier. On the contrary, the correlation is more pronounced for the  $R_1$  configurations, where the atoms that sit closer to the substrate have a higher core-electron BE than those on the topmost layers. In addition to this, there is a clear correlation between core-level shifts and Bader charge calculated for each of the atoms in  $Pt_{12}$  and  $Pt_{13}$  clusters in the different  $R_1$ – $R_4$  configurations. This result is shown in Figure 3b, and it reveals that the atoms with the highest core-electron BEs possess positive Bader charge up to 0.25e. Conversely, the atoms with the lowest BEs display an electron surplus with a total negative charge up to  $-0.18e$ .

For the comparison of experimental and theoretical results in the oxygen adsorption process, we have thus decided to consider only the  $R_1$  configurations of minimum energy for  $Pt_{12}$  and  $Pt_{13}$ . We expect these configurations to be the most representative among the clusters deposited on our substrate.

We performed calculations by varying the number  $m$  of oxygen atoms per cluster for  $m = 2, 4, 6$ , and 8. We also included in the calculations the structures with the stoichiometry  $Pt_nO_m$ , which are the most stable gas-phase structures for clusters of this size.<sup>[65]</sup> The geometric structure of the minimum energy clusters is shown in Figure 4, along with the result of the spectral fitting derived from the data analysis.

From a geometrical perspective,  $Pt_{12}$  and  $Pt_{13}$  behave in a very similar way up to  $m = 4$ . Oxygen is mostly adsorbed in bridge sites or, more rarely, in asymmetric threefold sites where one of the Pt–O bond lengths is shorter than the remaining two, in agreement with previous reports.<sup>[66]</sup> For  $m = 4$ , the O adsorption induces the formation of a zigzag oxide stripe on the upper side of the cluster. The stripe consists of three successive linear O–Pt–O subunits interconnected at an angle of  $\approx 80^\circ$  (see inset in Figure 4). For both  $Pt_{12}$  and  $Pt_{13}$ , the Pt–O bond length is shorter at the edges of the stripe (1.93 Å) and longer in the inner

part (2.02 Å). For  $m = 6$ , the two clusters start behaving differently, with only  $Pt_{12}$  undergoing a strong structural rearrangement. Finally, when they reach the stoichiometry  $Pt_mO_m$ , they both assume a highly distorted structure where the topmost part of the clusters is rich in Pt atoms bonded with four O atoms and an average Pt–O bond length of 2.01 ( $Pt_{12}$ ) and 1.98 Å ( $Pt_{13}$ ).

Analogously to what has been carried out for the clean clusters, we calculated the CLS of each atom ( $R_1$  cluster configuration) also for those bonded to an increasing number of O atoms, as shown in Figure 4. As observed in the experimental spectra plotted in Figure 1d,e and similarly to the case of Pt(111) surfaces (Figure 1f), oxygen adsorption leads to a shift of the  $4f$  core levels toward higher BE. Like the trend observed for surfaces of many transition metals,<sup>[67–70]</sup> the CLS also exhibits a linear dependence on the oxygen coverage (see Figure S7, Supporting Information),  $\approx 80$  meV  $O^{-1}$  atom.

The results from the spectral analysis plotted in Figure 4 show that despite the variations in oxygen density being included in the calculations, it is not possible to obtain a fit with an acceptable residual. For both  $Pt_{12}$  and  $Pt_{13}$ , the residuals are consistently much worse than those obtained for clean clusters. In fact, the two-component spin-orbit split structure that stems from the experimental analysis is not reproduced by any theoretical calculation.

For both clusters, the components with lower BE (72.03 and  $71.86 \pm 0.10$  eV for  $Pt_{12}$  and  $Pt_{13}$ , respectively) match the barycenter of the BEs of the two clusters with  $m = 4$  adsorbed O atoms (71.91 and 71.96 eV). However, the second component in the experimental spectra shows BEs ( $73.21$  and  $72.94 \pm 0.10$  eV, for  $Pt_{12}$  and  $Pt_{13}$ , respectively) that, according to our calculations, are greater than those of the  $Pt_nO_n$  clusters (72.6 and 72.7 eV for  $n = 12$  and 13, respectively). Therefore, a direct comparison between theory and experiment would suggest that the system is composed partly of clusters with low oxygen density ( $m = 4$ ) and partly of others with extremely high coverage ( $m > n$ ), without intermediate compositions. Such a result is not reasonable from a statistical point of view.

We then followed a different strategy, attempting to place the oxygen atoms, even for intermediate coverage, nonhomogeneously on the cluster, for instance, densifying them on the upper part of the surface ( $Pt_nO_m^{\text{top}}$ ) or around their base ( $Pt_nO_m^{\text{bot}}$ ), close to the interface with graphene. The surprising result, reported in Figure 5a, is that the two arrangements of oxygen atoms lead to very different simulated spectra (see bar codes represented in different colors). Particularly, the fit with the CLS of the oxygen configuration with atoms adsorbed on the upper part of the clusters (geometry shown in Figure 5b) returns a markedly lower chi-square (see Table S1, Supporting Information) compared to that of the homogeneous distribution or the one with oxygen on the lower part of the cluster.  $Pt_6O_{13}^{\text{top}}$  fits well the experimental spectrum of the oxidized  $Pt_{13}$  cluster, and a similar result applies to  $Pt_{12}$ , where the only difference is that to fit the data it is necessary to use a combination of  $Pt_{12}O_m^{\text{top}}$  with  $m = 6$  and 8.

The  $Pt_nO_m^{\text{top}}$  clusters exhibit very similar structures. For  $m = 6$ , a Pt atom on the topmost layer adopts the local  $PtO_4$  squared planar motif with a Pt atom at the center of 4 O atoms (see Figure 5b) typical of  $PtO$  and  $Pt_3O_4$  bulk oxides,<sup>[71]</sup> while a second Pt atom binds to three oxygen atoms. The average Pt–O

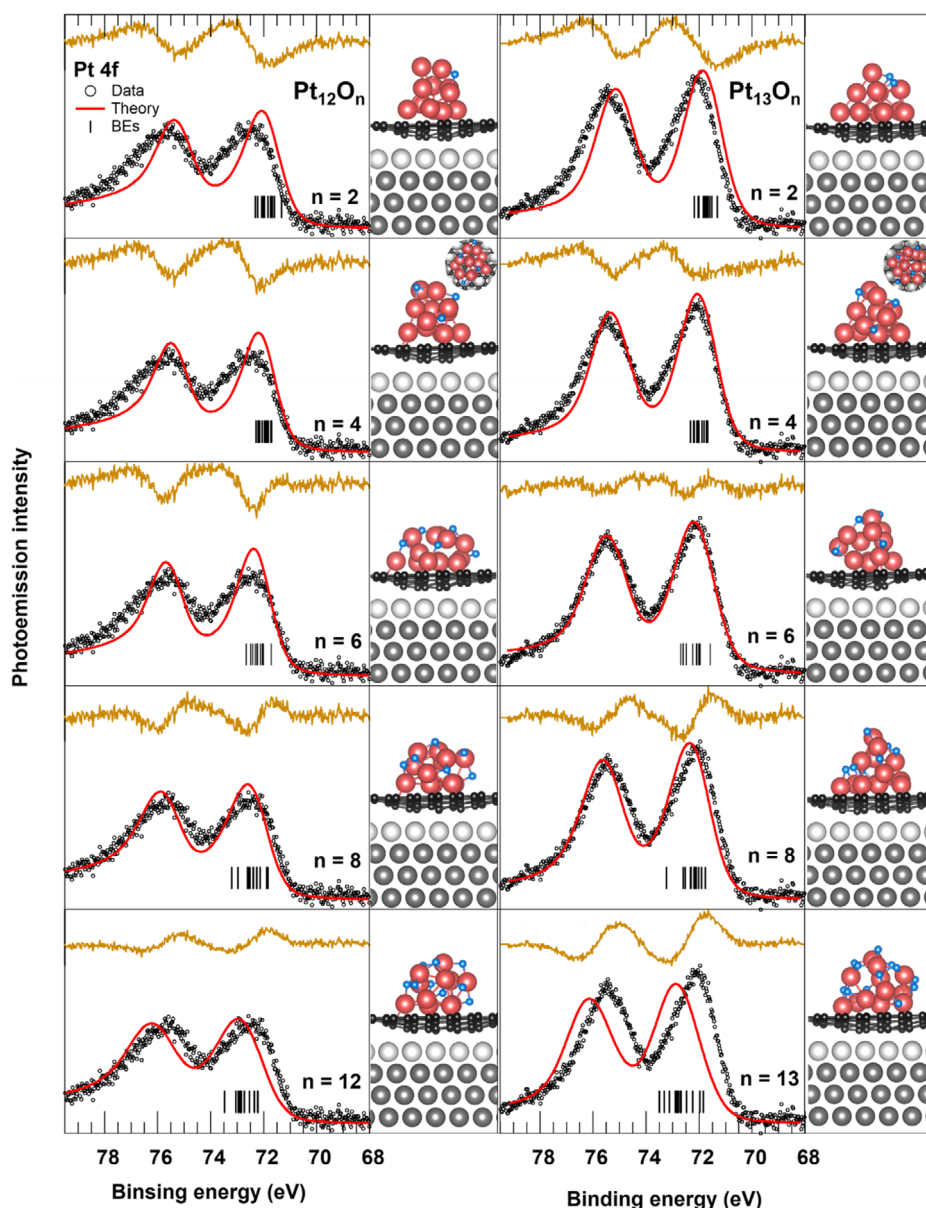


**Figure 4.** Pt 4f core-level spectra for clusters formed by 12 (left column) and 13 (right column) Pt atoms, onto which oxygen was adsorbed using a photodissociative process.  $m$  is the number of oxygen atoms bonded to each cluster. The fits of the spectra, obtained using the results of DFT ( $4f_{7/2}$  BEs are shown in bar code in each panel—one segment for each atom of the cluster), are indicated by red curves. It is noteworthy that the spectra of the residuals (brown curve) consistently show considerable modulation (see Table S1, Supporting Information).

bond length for the first Pt atom in both  $\text{Pt}_{12}$  and  $\text{Pt}_{13}$  is 1.97 Å, while for the second atom, it decreases to 1.86 Å. Regarding  $m = 8$ , which was only investigated for  $\text{Pt}_{12}$  since  $m = 6$  was adequate to fit the experimental spectra of  $\text{Pt}_{13}$ , a similar structure to  $m = 6$  is observed, but with an additional oxygen atom on each side of the cluster. However, the mechanism that leads the oxygen atom to have a higher probability of being adsorbed on the top part of the cluster is still to be explained. To address this issue, we first decided to evaluate the interaction energy of an  $\text{O}_2$  molecule as a function of its distance from the graphene layer, at a distance sufficiently large not to be affected by the presence

of the Pt cluster. The trend of the energy, shown in **Figure 6**, follows a typical physisorption interaction behavior with a minimum energy of 140 meV at 3.15 Å from the carbon layer. This value is comparable to that obtained in the case of oxygen physisorption on graphene<sup>[72]</sup> or on graphite surfaces.<sup>[73]</sup> However, it is important to note that the distance of the  $\text{O}_2$  molecule with respect to the Pt atoms forming the cluster is strongly affected by the pinning process of the graphene. If we evaluate such quantity, we see that the minimum of the curve is located around the second atomic layer of the cluster. Given the minimal variation in the potential energy curve  $\text{O}_2$ –graphene distance larger than

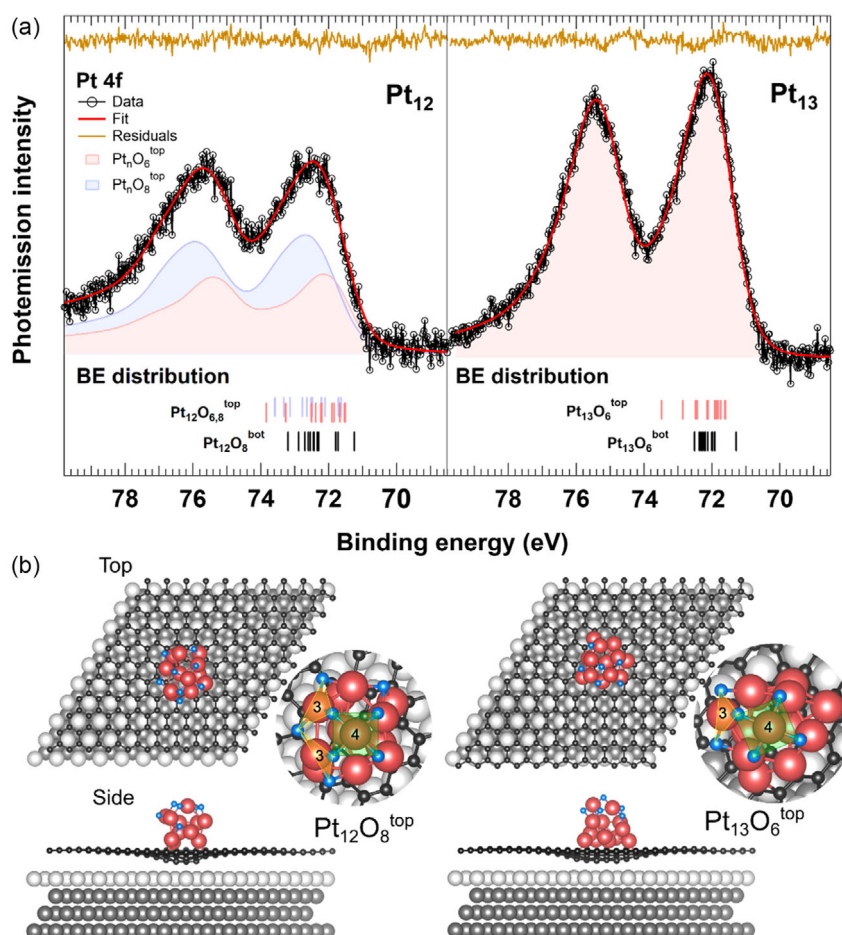


**Figure 5.** a) High-resolution Pt 4f core-level spectrum for oxidized Pt<sub>12</sub> and Pt<sub>13</sub>. The red lines through the spectra are the results of the linear least-square fits to the data points. The residuals of the fit are also shown in the top part of the panels (brown curves). Calculated DFT core-electron BEs are reported as bar codes. b) Corresponding top and side views of the structural models of the configurations that provide the best agreement in the spectral comparison between experiment and theory are shown. The insets highlight the Pt atoms bonded with 4 and 3 O atoms and the squared (green) and triangular (yellow) motifs.

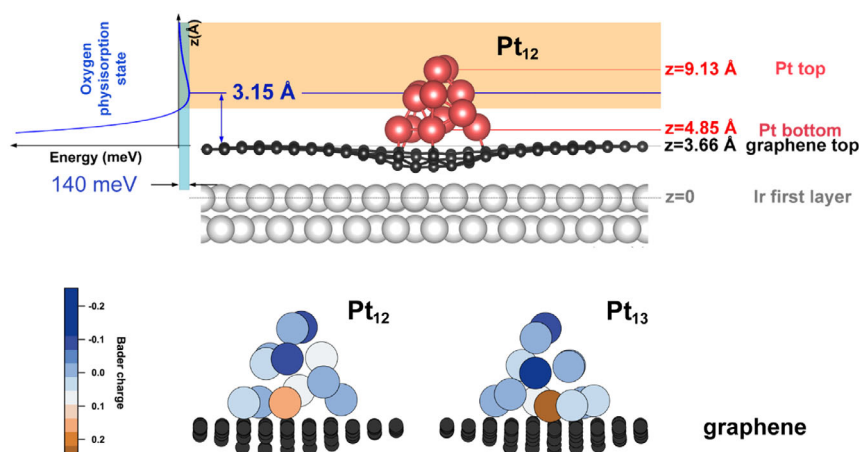


**Figure 6.** Side view of the Pt<sub>12</sub> cluster adsorbed on GR/Ir(111), highlighting the minimum in the curve of molecular oxygen adsorption on graphene and the distances between the different layers of C and Pt with respect to the first atomic layer of the Ir substrate. The orange-colored band defines the space where there is a higher probability of finding a molecule of O<sub>2</sub> physisorbed on graphene. The bottom panel shows the electronic charge redistribution in both Pt<sub>12</sub> and Pt<sub>13</sub>.



3.15 Å and considering that the mobility of a physisorbed molecule is very high in the direction parallel to graphene, we can assume that there is a high density of oxygen molecules physisorbed at distances greater than 3.15 Å from the carbon layer, which correspond to 8–9 Å from the Ir surface (orange band). The high density and the ability to diffuse thus lead to enhanced O<sub>2</sub> physisorption on the top part of the cluster.

Besides this diffusion process above graphene, which can enhance the sticking probability on the top side of the cluster, the reduced coordination number<sup>[6]</sup> and other electronic properties associated with the charge transfer at the interface<sup>[59,62]</sup> could make the atoms on the top part more active sites. As reported in the bottom part of Figure 6, the calculated Bader charge in Pt<sub>12</sub> and Pt<sub>13</sub> shows a negative charge surplus in the undercoordinated atoms sitting far away from the interface with graphene. On the contrary, the Pt atoms at the cluster–graphene interface result partially oxidized as they possess a cumulative positive charge of +0.18e and +0.35e for Pt<sub>12</sub> and Pt<sub>13</sub>, respectively. A similar charge redistribution was observed also for Pt clusters supported on oxides such as Co<sub>3</sub>O<sub>4</sub> and TiO<sub>2</sub>, on which Pt atoms directly bind to oxygen.<sup>[65]</sup> In particular, both clusters contain one atom at the interface with graphene possessing a much higher positive charge compared to the others, which goes up to 0.25e for Pt<sub>13</sub>. This high charge is due to the combination of two effects which both contribute to an increasing positive charge: the low distance from the graphene, as discussed in the present work, and the fact that these atoms are those with the highest coordination number, which also contributes to a higher positive charge with respect to the undercoordinated atoms in the outer layers.<sup>[74]</sup> Another interesting aspect is the different oxygen coverage in the two clusters, which is notably higher for the cluster composed of 12 atoms. We link this result to the geometric reconstruction that takes place in the topmost layer of the clusters, which is known to play a pivotal role in the O<sub>2</sub> adsorption process on Pt nanoclusters.<sup>[75]</sup> In the case of Pt<sub>12</sub>, when the oxygen density increases, the two atoms that occupy the topmost layer in the metallic phase change their local configuration. In particular, one of the two atoms moves toward the second atomic layer of the cluster, decreasing the coordination number of the other atom left behind, with a consequent change in the local density of states and Bader charge.<sup>[72,73]</sup> At the same time, the atom that moved to the second layer has a distance from graphene (≈3.2 Å) still accessible for the physisorbed molecular O<sub>2</sub>. On the contrary, in the case of Pt<sub>13</sub>, this reconstruction takes place only for larger coverages (see Figure 4), while the two atoms in the topmost layer are preserving their local configuration for lower oxygen densities and in particular for  $m = 6$  adsorbed oxygen atoms, which is the configuration that better fits the experimental spectrum. This interpretation is in agreement with previous calculations that predict that smaller Pt clusters are easier to oxidize<sup>[65]</sup> and that Pt<sub>12</sub> is more reactive than Pt<sub>13</sub> as a result of an electronic structure that fluctuates to a greater extent compared to Pt<sub>13</sub>.<sup>[77]</sup>

The molecular diffusion process onto graphene toward the clusters closely resembles the reverse spillover phenomenon observed on oxide surfaces used in catalysis. This phenomenon entails molecular species chemisorbing onto the catalyst surface after being trapped and diffusing onto oxide surfaces.<sup>[78]</sup> Our analysis first highlights that structural alterations induced

by the graphene-pinning process stimulate the molecular adsorption of O<sub>2</sub> onto cluster surfaces and its subsequent photoinduced dissociation. Although we have shown that this process occurs at low temperature, such an outcome is valid also at temperatures relevant for catalysis ( $T > 350$  K), at which oxygen can directly adsorb onto nanoclusters in a dissociative manner, albeit passing through a physisorption state. Second, the distinct Bader charge exhibited by atoms in the top layer of Pt cluster supported by graphene can significantly influence and bolster processes of adsorption and molecular recombination.

### 3. Conclusion

In summary, our investigation into the adsorption and photodissociation mechanisms of molecular oxygen on mass-selected Pt<sub>12</sub> and Pt<sub>13</sub> clusters deposited onto graphene/Ir(111) surfaces unveils a targeted oxidation occurring primarily on the surface layer of the clusters. This finding is closely tied to the highly synergistic behavior inherent in the graphene corrugation process, with the support playing a protagonist role in the oxidation of the clusters. The pristine corrugation of the graphene/Ir(111) interface induces the trapping of metallic clusters in specific lattice regions, closer to the Ir(111) surface. Simultaneously, the cluster adsorption process, guided by interactions with the substrate, leads to an increased corrugation of graphene (pinning). This indirectly affects atomic and molecular adsorption properties, consequently influencing chemical reactivity as in our case. It is crucial to underscore that the interaction between clusters and the substrate, particularly the electronic charge redistribution on the Pt clusters, plays a fundamental role in this synergistic effect. This insight suggests a potential avenue for tuning the interaction of clusters with specific adsorbents or achieving selective adsorption onto different sites.

As it has been widely demonstrated in the case of Pt nanoparticles<sup>[37,79]</sup> and single-atom catalysts,<sup>[41]</sup> we expect that the ability to obtain geometric information about oxygen adsorption on ultrasmall Pt clusters could be of paramount importance to improve the strategy for an experimental-supported design of catalysts.

### 4. Experimental Section

**Substrate Preparation:** An Ir(111) single crystal was cleaned by repeated cycles of Ar<sup>+</sup> sputtering and annealing in an O<sub>2</sub> atmosphere between 800 and 1100 K. The residual oxygen was removed by final flash annealing up to 1500 K. Graphene was grown by cycles of ethylene dosing at  $5 \times 10^{-7}$  mbar onto the Ir(111) surface kept at 520 K followed by annealing to 1470 K. The sample quality was checked by means of low-energy electron diffraction (LEED) and photoemission from the C 1s and the Ir 4f<sub>7/2</sub> core levels. The graphene sample showed sharp LEED spots with the characteristic Moiré pattern typical of a single-domain graphene on the Ir(111) substrate.

**Pt Cluster Deposition:** Pt<sub>12</sub><sup>+</sup> and Pt<sub>13</sub><sup>+</sup> positive clusters were produced using the cluster source Exact Number of Atoms in each Cluster. In this source, clusters were generated starting from the laser ablation of a metal target. The mass selection was performed with a quadrupole mass analyzer. A more detailed description of the source was reported elsewhere.<sup>[42,80]</sup> The Pt<sub>n</sub><sup>+</sup> clusters were deposited on graphene/Ir(111), on which they were electrically neutralized. The amount of clusters reaching the surface was monitored by directly reading the current on the sample,



on which we applied a positive voltage to reduce the kinetic energy  $E_k$  of the clusters, thus ensuring soft landing conditions (i.e.,  $E_k < 1$  eV per atom).<sup>[81,82]</sup> The cluster density was below  $9 \times 10^{-3}$  cluster per nm<sup>2</sup>, and the temperature of the sample was kept at 20 K during the deposition, reaction, and measurements to avoid cluster sintering.

**HR-XPS:** HR-XPS measurements were performed in situ at the SuperESCA beamline of the synchrotron-radiation facility Elettra (Trieste, Italy). The photoemission spectra were collected by means of a Phoibos 150 mm mean-radius hemispherical electron energy analyzer (SPECS). The overall energy resolution was better than 50 meV for the photon energies and acquisition parameters employed. The XPS spectra were acquired by tuning the photon energy for having a photoelectron kinetic energy of about 100 eV, to enhance surface sensitivity. For each spectrum, the photoemission intensity was normalized to the photon flux, and the BE scale was aligned to the Fermi energy of the Ir substrate. For the fitting procedure of the core levels, a Doniach–Šunjić<sup>[83]</sup> line profile was used for each spectral component, convoluted with a Gaussian distribution to account for the experimental, phonon, and inhomogeneous broadening. The Doniach–Šunjić profile contained a Lorentzian distribution arising from the finite core-hole lifetime and an asymmetry parameter  $\alpha$  for electron–hole pair excitations near the Fermi level. Line shape parameters obtained were based on least-square fit. Fit quality was quantitatively assessed by evaluation of the chi-square and of the residuals, which should exhibit no systematic deviations and show only the fluctuation due to counting statistics.

## 5. Theoretical Section

The calculations were performed using DFT as implemented in the Vienna Ab-initio Simulation Package (VASP) code.<sup>[84]</sup> The systems were described with a slab with four layers of Ir in a  $(9 \times 9)$  hexagonal supercell and a layer of  $(10 \times 10)$  unit cells of graphene placed on top with an overall number of 524 atoms, excluding the Pt<sub>12</sub> and Pt<sub>13</sub> cluster. The starting cluster geometry was the minimum energy configuration structure that Pt<sub>12</sub><sup>+</sup> and Pt<sub>13</sub><sup>+</sup> adopted in the gas phase.

The Pt clusters were placed as neutral species, because of charge neutralization by graphene, on the valley of the weakly corrugated graphene layer, with his center on an HCP site, where the stronger interaction with the Ir(111) substrate was known to increase its stability. The bottom two layers of Ir were kept frozen at their bulk geometry, with a lattice parameter of 2.74 Å, and the rest of the system (Pt cluster included) was fully relaxed using the rev-vdw-DF2 functional<sup>[85]</sup> until the largest residual force was less than 0.015 eV Å<sup>-1</sup>. The vacuum distance between the two surfaces of the periodically repeated slabs was at least 9.5 Å for the Pt cluster-covered surface. We employed the projector augmented method (PAW)<sup>[86]</sup> using perdew-burke-ernzerhof (PBE)<sup>[87]</sup> potentials. The plane wave cutoff was set to 400 eV, and the relaxations were performed by sampling the Brillouin zone using the  $\Gamma$  point only. Core-level BEs were obtained as the difference in energy from a first standard calculation and a second one in which a core electron was removed from an atom and placed in valence. This can be achieved by creating a new pseudopotential for the atom with the core hole and adding one electron to the total number of valence electrons. In the PAW formalism employed in VASP, this was done during the calculation, without the need to explicitly generate a separate PAW for the atom with the hole in the core. In both calculations, the total charge density was driven to self-consistency, thereby considering the relaxation of the valence electrons around the hole. The residual core electrons were kept frozen, and so their screening was neglected. This was commonly known as the “final state” approximation. Using this approach, only differences in core-level BEs can be compared with the corresponding measurable quantities. To this purpose, absolute core-level BEs were shifted using an offset parameter which was included in the fitting procedure and allowed to vary until the best fit with the experiment was found.

## Supporting Information

Supporting Information is available from the Wiley Online Library or from the author.

## Acknowledgements

A.B. gratefully acknowledges the financial support from the National Quantum Science and Technology Institute (PNRR MUR project PE0000023-NQSTI). D.A. was supported by the Natural Environment Research Council (grant no. NE/R000425/1). This work used the ARCHER2 UK National Supercomputing Service (<https://www.archer2.ac.uk>). A.B. and D.A. acknowledge MUR for the support of the PRIN Project no. 20222FXZ33 entitled “Materials modelling for energy storage applications”. F.L. thanks the support provided for the finalization of the work by the project named Scientific excellence in Nano-CATalysis at the Heyrovský Institute (acronym NanoCAT) which was funded by the European Union under grant agreement number 101079142 within the Horizon Europe Framework Programme under the CALL: HORIZON-WIDERA-2021-ACCESS-03. The authors acknowledge Elettra Sincrotrone Trieste for providing access to its synchrotron radiation facilities and for financial support. The authors thank Prof. S. Vajda for stimulating discussions and critical reading of the manuscript.

Open access publishing facilitated by Università degli Studi di Trieste, as part of the Wiley - CRUI-CARE agreement.

## Conflict of Interest

The authors declare no conflict of interest.

## Data Availability Statement

The data that support the findings of this study are available from the corresponding author upon reasonable request.

## Keywords

clusters, density functional theories, graphenes, platinum, X-ray photoelectron spectroscopies

Received: May 21, 2024

Revised: June 29, 2024

Published online:

- [1] T. Zambelli, J. Winterlin, J. Trost, G. Ertl, *Science* **1996**, 273, 1688.
- [2] B. Goris, S. Bals, W. Van den Broek, E. Carbó-Argibay, S. Gómez-Graña, L. M. Liz-Marzán, G. Van Tendeloo, *Nat. Mater.* **2012**, 11, 930.
- [3] F. Baletto, R. Ferrando, *Rev. Mod. Phys.* **2005**, 77, 3713.
- [4] J. Resasco, L. DeRita, S. Dai, J. P. Chada, M. Xu, X. Yan, J. Finzel, S. Hanukovich, A. S. Hoffman, G. W. Graham, S. R. Bare, X. Pan, P. Christopher, *J. Am. Chem. Soc.* **2020**, 142, 169.
- [5] F. R. Negreiros, A. Halder, C. Yin, A. Singh, G. Barcaro, L. Sementa, E. C. Tyo, M. J. Pellin, S. Bartling, K.-H. Meiwes-Broer, S. Seifert, P. Sen, S. Nigam, C. Majumder, N. Fukui, H. Yasumatsu, S. Vajda, A. Fortunelli, *Angew. Chem. Int. Ed.* **2018**, 57, 1209.
- [6] C. Yin, F. R. Negreiros, G. Barcaro, A. Beniya, L. Sementa, E. C. Tyo, S. Bartling, K.-H. Meiwes-Broer, S. Seifert, H. Hirata, N. Isomura, S. Nigam, C. Majumder, Y. Watanabe, A. Fortunelli, S. Vajda, *J. Mater. Chem. A* **2017**, 5, 4923.
- [7] B. Yang, C. Liu, A. Halder, E. C. Tyo, A. B. F. Martinson, S. Seifert, P. Zapol, L. A. Curtiss, S. Vajda, *J. Phys. Chem. C* **2017**, 121, 10406.

- [8] H. Rong, S. Ji, J. Zhang, D. Wang, Y. Li, *Nat. Commun.* **2020**, *11*, 5884.
- [9] E. C. Tyo, S. Vajda, *Nat. Nanotechnol.* **2015**, *10*, 577.
- [10] L. Liu, A. Corma, *Chem. Rev.* **2018**, *118*, 4982.
- [11] J. Lee, P. Tieu, J. Finzel, W. Zang, X. Yan, G. Graham, X. Pan, P. Christopher, *J. Am. Chem. Soc.* **2023**, *3*, 2299.
- [12] W. He, X. Zhang, K. Zheng, C. Wu, Y. Pan, H. Li, L. Xu, R. Xu, W. Chen, Y. Liu, C. Wang, Z. Sun, S. Wei, *Angew. Chem. Int. Ed.* **2023**, *62*, e202213365.
- [13] A. I. Stadnichenko, E. M. Slavinskaya, O. A. Stonkus, A. I. Boronin, *ChemCatChem* **2024**, e202301727.
- [14] S. Das, U. Anjum, K. H. Lim, Q. He, A. S. Hoffman, S. R. Bare, S. M. Kozlov, B. C. Gates, S. Kawi, *Small* **2023**, *19*, 2207272.
- [15] B. Zhang, Y. Chen, J. Wang, H. Pan, W. Sun, *Adv. Funct. Mater.* **2022**, *32*, 2202227.
- [16] Y. Zhao, P. V. Kumar, X. Tan, X. Lu, X. Zhu, J. Jiang, J. Pan, S. Xi, H. Y. Yang, Z. Ma, T. Wan, D. Chu, W. Jiang, S. C. Smith, R. Amal, Z. Han, X. Lu, *Nat. Commun.* **2022**, *13*, 2430.
- [17] W. Chen, X. Zhu, W. Wei, H. Chen, T. Dong, R. Wang, M. Liu, K. Ostrikov, P. Peng, S.-Q. Zang, *Small* **2023**, *19*, 2304294.
- [18] L. DeRita, S. Dai, K. Lopez-Zepeda, N. Pham, G. W. Graham, X. Pan, P. Christopher, *J. Am. Chem. Soc.* **2017**, *139*, 14150.
- [19] W. Zang, J. Lee, P. Tieu, X. Yan, G. W. Graham, I. C. Tran, P. Wang, P. Christopher, X. Pan, *Nat. Commun.* **2024**, *15*, 998.
- [20] L. DeRita, J. Resasco, S. Dai, A. Boubnov, H. V. Thang, A. S. Hoffman, I. Ro, G. W. Graham, S. R. Bare, G. Pacchioni, X. Pan, P. Christopher, *Nat. Mater.* **2019**, *18*, 746.
- [21] B. Zhang, G. Sun, S. Ding, H. Asakura, J. Zhang, P. Sautet, N. Yan, *J. Am. Chem. Soc.* **2019**, *141*, 8185.
- [22] A. Wang, J. Li, T. Zhang, *Nat. Rev. Chem.* **2018**, *2*, 65.
- [23] W. Guo, Z. Wang, X. Wang, Y. Wu, *Adv. Mater.* **2021**, *33*, 2004287.
- [24] S. Vajda, M. J. Pellin, J. P. Greeley, C. L. Marshall, L. A. Curtiss, G. A. Ballentine, J. W. Elam, S. Catillon-Mucherie, P. C. Redfern, F. Mehmood, P. Zapol, *Nat. Mater.* **2009**, *8*, 213.
- [25] E. T. Baxter, M.-A. Ha, A. C. Cass, A. N. Alexandrova, S. L. Anderson, *ACS Catal.* **2017**, *7*, 3322.
- [26] Z. Zhang, T. Masubuchi, P. Sautet, S. L. Anderson, A. N. Alexandrova, *Angew. Chem. Int. Ed.* **2023**, *62*, e202218210.
- [27] S. Kumari, T. Masubuchi, H. S. White, A. Alexandrova, S. L. Anderson, P. Sautet, *J. Am. Chem. Soc.* **2023**, *145*, 5834.
- [28] S. Proch, M. Wirth, H. S. White, S. L. Anderson, *J. Am. Chem. Soc.* **2013**, *135*, 3073.
- [29] C. Mager-Maury, G. Bonnard, C. Chizallet, P. Sautet, P. Raybaud, *ChemCatChem* **2011**, *3*, 200.
- [30] C. H. Hu, C. Chizallet, C. Mager-Maury, M. Corral-Valero, P. Sautet, H. Toulhoat, P. Raybaud, *J. Catal.* **2010**, *274*, 99.
- [31] T. Avanesian, S. Dai, M. J. Kale, G. W. Graham, X. Pan, P. Christopher, *J. Am. Chem. Soc.* **2017**, *139*, 4551.
- [32] F. Calle-Vallejo, J. Tymoczko, V. Colic, Q. H. Vu, M. D. Pohl, K. Morgenstern, D. Loffreda, P. Sautet, W. Schuhmann, A. S. Bandarenka, *Science* **2015**, *350*, 185.
- [33] J. Carnis, L. Gao, S. Fernández, G. Chahine, T. U. Schüllli, S. Labat, E. J. M. Hensen, O. Thomas, J. P. Hofmann, M.-I. Richard, *Small* **2021**, *17*, 2007702.
- [34] D. Kim, M. Chung, J. Carnis, S. Kim, K. Yun, J. Kang, W. Cha, M. J. Cherukara, E. Maxey, R. Harder, K. Sasikumar, S. K. R. S. Sankaranarayanan, A. Zozulya, M. Sprung, D. Riu, H. Kim, *Nat. Commun.* **2018**, *9*, 3422.
- [35] R. Mom, L. Frevel, J.-J. Velasco-Vélez, M. Plodinec, A. Knop-Gericke, R. Schlögl, *J. Am. Chem. Soc.* **2019**, *141*, 6537.
- [36] N. Seriani, in *Platinum Oxides in Heterogenous Catalysis: Simulation of Thermodynamic and Chemical Properties*, VDM Verlag Dr. Mueller e.K. **2008**, ISBN-10: 3639055268.
- [37] G. N. Vayssilov, Y. Lykhach, A. Migani, T. Staudt, G. P. Petrova, N. Tsud, T. Skála, A. Bruix, F. Illas, K. C. Prince, V. Matolín, K. M. Neyman, J. Libuda, *Nat. Mater.* **2011**, *10*, 310.
- [38] H. Wang, J.-X. Liu, L. F. Allard, S. Lee, J. Liu, H. Li, J. Wang, J. Wang, S. H. Oh, W. Li, M. Flytzani-Stephanopoulos, M. Shen, B. R. Goldsmith, M. Yang, *Nat. Commun.* **2019**, *10*, 3808.
- [39] A. Beniya, S. Higashi, N. Ohba, R. Jinnouchi, H. Hirata, Y. Watanabe, *Nat. Commun.* **2020**, *11*, 1888.
- [40] Y. Hang Li, J. Xing, Z. Jia Chen, Z. Li, F. Tian, L. Rong Zheng, H. Feng Wang, P. Hu, H. Jun Zhao, H. Gui Yang, *Nat. Commun.* **2013**, *4*, 2500.
- [41] P. Christopher, *ACS Energy Lett.* **2019**, *4*, 2249.
- [42] F. Loi, M. Pozzo, L. Sbuelz, L. Bignardi, P. Lacovig, E. Tosi, S. Lizzit, A. Kartouzian, U. Heiz, D. Alfé, A. Baraldi, *J. Mater. Chem. A* **2022**, *10*, 14594.
- [43] T. Imaoka, H. Kitazawa, W.-J. Chun, S. Omura, K. Albrecht, K. Yamamoto, *J. Am. Chem. Soc.* **2013**, *135*, 13089.
- [44] K. Yamamoto, T. Imaoka, W.-J. Chun, O. Enoki, H. Katoh, M. Takenaga, A. Sono, *Nat. Chem.* **2009**, *1*, 397.
- [45] T. Imaoka, H. Kitazawa, W.-J. Chun, K. Yamamoto, *Angew. Chem. Int. Ed.* **2015**, *54*, 9810.
- [46] L. Bianchettin, A. Baraldi, S. de Gironcoli, E. Vesselli, S. Lizzit, L. Petaccia, G. Comelli, R. Rosei, *J. Chem. Phys.* **2008**, *128*, 114706.
- [47] W. E. Kaden, T. Wu, W. A. Kunkel, S. L. Anderson, *Science* **2009**, *326*, 826.
- [48] D. Perco, F. Loi, L. Bignardi, L. Sbuelz, P. Lacovig, E. Tosi, S. Lizzit, A. Kartouzian, U. Heiz, A. Baraldi, *Commun. Chem.* **2023**, *6*, 61.
- [49] A. von Weber, E. T. Baxter, S. Proch, M. D. Kane, M. Rosenfelder, H. S. White, S. L. Anderson, *Phys. Chem. Chem. Phys.* **2015**, *17*, 17601.
- [50] W. Eberhardt, P. Fayet, D. M. Cox, Z. Fu, A. Kaldor, R. Sherwood, D. Sondericker, *Phys. Rev. Lett.* **1990**, *64*, 780.
- [51] C. Puglia, A. Nilsson, B. Hernnäs, O. Karis, P. Bennich, N. Mårtensson, *Surf. Sci.* **1995**, *342*, 119.
- [52] D. J. Miller, H. Öberg, S. Kaya, H. Sanchez Casalongue, D. Friebe, T. Anniyev, H. Ogasawara, H. Bluhm, L. G. M. Pettersson, A. Nilsson, *Phys. Rev. Lett.* **2011**, *107*, 195502.
- [53] L. K. Ono, J. R. Croy, H. Heinrich, B. Roldan Cuenya, *J. Phys. Chem. C* **2011**, *115*, 16856.
- [54] J. G. Wang, W. X. Li, M. Borg, J. Gustafson, A. Mikkelsen, T. M. Pedersen, E. Lundgren, J. Weissenrieder, J. Klikovits, M. Schmid, B. Hammer, J. N. Andersen, *Phys. Rev. Lett.* **2005**, *95*, 256102.
- [55] Z. Zhu, F. Tao, F. Zheng, R. Chang, Y. Li, L. Heinke, Z. Liu, M. Salmeron, G. A. Somorjai, *Nano Lett.* **2012**, *12*, 1491.
- [56] T. Gerber, J. Knudsen, P. J. Feibelman, E. Grånäs, P. Stratmann, K. Schulte, J. N. Andersen, T. Michely, *ACS Nano* **2013**, *7*, 2020.
- [57] A. T. N'Diaye, T. Gerber, C. Busse, J. Mysliveček, J. Coraux, T. Michely, *New J. Phys.* **2009**, *11*, 103045.
- [58] P. J. Feibelman, *Phys. Rev. B* **2008**, *77*, 165419.
- [59] Y. Du, D. Yi, X. Wang, *Carbon* **2022**, *192*, 295.
- [60] D. Yi, W. Zhao, F. Ding, *ACS Appl. Nano Mater.* **2019**, *2*, 2921.
- [61] J. Bord, B. Kirchhoff, M. Baldofski, C. Jung, T. Jacob, *Small* **2023**, *19*, 2207484.
- [62] X.-F. Li, F.-Y. Su, L.-J. Xie, Y.-R. Tian, Z.-L. Yi, J.-Y. Cheng, C.-M. Chen, *Small* **2024**, *23*, 2310940.
- [63] A. Baraldi, *J. Phys. Condens. Matter* **2008**, *20*, 093001.
- [64] J. Knudsen, P. J. Feibelman, T. Gerber, E. Grånäs, K. Schulte, P. Stratmann, J. N. Andersen, T. Michely, *Phys. Rev. B* **2012**, *85*, 035407.
- [65] M. Taleblou, M. F. Camellone, S. Fabris, S. Piccinin, *J. Phys. Chem. C* **2022**, *126*, 10880.
- [66] T. Jacob, R. P. Muller, W. A. Goddard, *J. Phys. Chem. B* **2003**, *107*, 9465.

- [67] A. Baraldi, S. Lizzit, G. Comelli, M. Kiskinova, R. Rosei, K. Honkala, J. K. Nørskov, *Phys. Rev. Lett.* **2004**, 93, 046101.
- [68] S. Lizzit, A. Baraldi, A. Groso, K. Reuter, M. V. Ganduglia-Pirovano, C. Stampfl, M. Scheffler, M. Stichler, C. Keller, W. Wurth, D. Menzel, *Phys. Rev. B* **2001**, 63, 205419.
- [69] M. V. Ganduglia-Pirovano, M. Scheffler, A. Baraldi, G. Comelli, G. Paolucci, R. Rosei, *Phys. Rev. B* **2001**, 63, 205415.
- [70] E. Miniussi, M. Pozzo, T. O. Montes, N. A. Nino, A. Locatelli, E. Vesselli, G. Comelli, S. Lizzit, A. Baraldi, *Carbon* **2014**, 73, 389.
- [71] J. E. Quinlivan Domínguez, K. M. Neyman, A. Bruix, *J. Chem. Phys.* **2022**, 157, 094709.
- [72] F. R. Bagsican, A. Winchester, S. Ghosh, X. Zhang, L. Ma, M. Wang, H. Murakami, S. Talapatra, R. Vajtai, P. M. Ajayan, J. Kono, M. Tonouchi, I. Kawayama, *Sci. Rep.* **2017**, 7, 1774.
- [73] A. S. Mohamed Ibrahim, S. Morisset, S. Baouche, F. Dulieu, *J. Chem. Phys.* **2022**, 156, 194307.
- [74] A. Ohnuma, K. Takahashi, H. Tsunoyama, T. Inoue, P. Zhao, A. Velloth, M. Ehara, N. Ichikuni, M. Tabuchi, A. Nakajima, *Catal. Sci. Technol.*, **2022**, 12, 1400.
- [75] H. Hirase, K. Iida, J.-y. Hasegawa, *Phys. Chem. Chem. Phys.* **2024**, 26, 18530.
- [76] Y. Watanabe, X. Wu, H. Hirata, N. Isomura, *Catal. Sci. Technol.* **2011**, 1, 1490.
- [77] K. Miyazaki, H. Mori, *Sci. Rep.* **2017**, 7, 45381.
- [78] M. A. Röttgen, S. Abbet, K. Judai, J.-M. Antonietti, A. S. Wörz, M. Arenz, C. R. Henry, U. Heiz, *J. Am. Chem. Soc.* **2007**, 129, 9635.
- [79] S. Mitchell, R. Qin, N. Zheng, J. Pérez-Ramírez, *Nat. Nanotechnol.* **2021**, 16, 129.
- [80] L. Sbuelz, F. Loi, M. Pozzo, L. Bignardi, E. Nicolini, P. Lacovig, E. Tosi, S. Lizzit, A. Kartouzian, U. Heiz, D. Alfé, A. Baraldi, *J. Phys. Chem. C* **2021**, 125, 9556.
- [81] C. Binns, *Surf. Sci. Rep.* **2001**, 44, 1.
- [82] S. J. Carroll, P. Weibel, B. V. Issendorff, L. Kuipers, R. E. Palmer, *J. Phys. Condens. Matter* **1996**, 8, L617.
- [83] S. Doniach, M. Sunjic, *J. Phys. C: Solid State Phys.* **1970**, 3, 285.
- [84] G. Kresse, J. Furthmüller, *Phys. Rev. B* **1996**, 54, 11169.
- [85] I. Hamada, *Phys. Rev. B* **2014**, 89, 121103.
- [86] P. E. Blöchl, *Phys. Rev. B* **1994**, 50, 17953.
- [87] J. P. Perdew, K. Burke, M. Ernzerhof, *Phys. Rev. Lett.* **1996**, 77, 3865.